Small Structures / Volume 5, Issue 6 / 2300540

Research Article | Open Access

Significance of the Different Exposed Surfaces of ZnO Single Crystals and Nanowires on the Photocatalytic Activity and Processes

Adrien Baillard, Estelle Appert, Laetitia Rapenne, Véronique Jacob, Alexandre Dieulesaint, Jean-Michel Chauveau, Vincent Consonni

First published: 12 April 2024
https://doi.org/10.1002/sstr.202300540

Abstract

The heterogeneous photocatalysis of organic dyes using ZnO nanowires (NWs) is of high interest to face the challenge of eco-efficient water remediation. However, the effects of the wurtzite structure of ZnO and hence of the shape of nanostructures on the photocatalytic processes are still under debate. Herein, it is shown that the photocatalytic activity of ZnO single crystals with five different orientations follows a pseudo-first-order kinetics as: $(000\bar{1})$ < $\{10\bar{1}2\}$ < $\{20\bar{2}1\}$ < $\{10\bar{1}0\}$ < (0001). The photocatalytic processes are independent of the nature of the crystallographic planes, apart from the semipolar $\{20\bar{2}1\}$ orientation. Interestingly, ZnO NWs exhibit a photocatalytic activity that is relatively independent of their length, which is neither due to the penetration of organic dyes nor to the penetration of UV light. Instead, the sidewalls of ZnO NWs are much less efficient than the ZnO single crystal with the same nonpolar *m*-plane orientation, indicating that the structural morphology and chemical composition of the surface, as well as their much higher doping level, govern the photocatalytic activity and processes. These findings indicate that the increase in the photocatalytic activity of ZnO NWs should be addressed by designing more active surfaces rather than simply increasing their total surface area.

1 Introduction

The quality of fresh water in Europe has made some progress over the last few years, but there are still significant efforts to make.[1] According to Persson et al. another planetary boundary has recently been overcome.[2] This planetary boundary is the one of novel entities that includes persistent organic pollutants (POPs) as organic dyes. The generation of new POPs still increases and human being is unfortunately not able to manage all the waste yet.[3] The development of green chemistry has thus become of high significance along with the treatment of chemicals already produced and to be produced in the near future.

In the present context, advanced oxidation processes (AOPs) have emerged as an efficient way among others to address the issue of POPs.[4] Following the approach of eliminating POPs, AOPs consist in generating highly reactive radicals including $^{\bullet}OH$ and $^{\bullet}O_2^-$ species to induce the degradation of pollutants.[5] The generation process can be helped by different media such as ozone,[6, 7] hydrogen peroxide,[8] Fenton's reagents,[9, 10] UV light or catalyst.[11, 12] In the framework of the photocatalysis concept, $^{\bullet}OH$ and $^{\bullet}O_2^-$ radicals are formed through the illumination of a semiconducting catalyst with a UV light ($E_{light} > E_{gap}$) generating electron/hole pairs reacting with molecules on their surfaces.[13] This concept was reported for the first time by Fuhishima and Honda in 1972, using TiO_2 illuminated under UV light for water splitting in hydrogen and oxygen species.[14] From thereon, different applications have emerged mainly focused on the use of reactive radicals for removing dyes and other organic pollutants from fresh water.

Among the different semiconducting catalysts such as TiO_2,[15] Cu_2O,[16] or Fe_2O_3,[17] ZnO as a biocompatible semiconductor[18] made of abundant elements has emerged as a highly promising candidate owing to its wide bandgap energy of 3.37 eV at room temperature.[12] It can further be grown as nanostructures with different shapes (e.g., nanoparticles, nanowires (NWs), nanorods (NRs), …) using surface scalable, low-cost, low-temperature chemical processes such as chemical bath deposition (CBD) and hydrothermal method.[19] ZnO typically crystallizes into the highly anisotropic wurtzite structure belonging to the 6 mm point group, which is both polar and piezoelectric along the <0001> direction (i.e., along the *c*-axis).[20] The hexagonal type lattice favors the existence of different polar, semipolar, and nonpolar planes, each of them exhibiting a specific surface atomic structure. The photocatalytic processes in ZnO are generally affected by the nature of planes on the surface of nano- and microstructures, and have been under intense debate.[21-23] Mclaren et al. proposed that the polar *c*-planes are more efficient than the nonpolar *m*-planes by comparing the photocatalytic activity of platelet-like and rod-shaped particles grown by a wet chemical route using zinc acetate dihydrate and oleic acid with different concentrations mixed in trioctylamine solvent.[21] However, the photocatalytic activity in the ZnO powder was compared for a similar weight without providing any information on the exposed surface areas. Using a similar powder approach, Han et al. reported that the photocatalytic activity follows the present hierarchy, () >

{} > {} and (), by investigating flakes, columns, and pyramids grown by a wet chemical route using different zinc precursors and additives in different solvents.[22] Only a small difference between the polar *c*- and nonpolar *m*-planes was reported as compared to McLaren et al.[21] In contrast, Liu et al. revealed an opposite behavior with a higher photocatalytic activity obtained from NRs than from platelets grown by a solvothermal method using zinc nitrate hexahydrate mixed in *N,N'* dimethylformamide/water solvent with different volumes, arising from the photocorrosion stability.[23] From the three studies, no consensus has emerged regarding the photocatalytic activity of ZnO powder since a large number of differences in the deposition techniques, growth procedures, and resulting properties of objects have been identified. In addition, other studies investigating the influence of the structural morphology have shown that the change of surface defects originating from the different deposition techniques and growth procedures play a major role in the photocatalytic activity.[24, 25] This may even be more significant than the nature of the exposed surface and its related area.[26] At the same time, Kislov et al. investigated the effect of the nature of the planes of ZnO on the photocatalytic activity using a single crystal approach. They compared the photocatalytic activity of ZnO single crystals with the (), (), and {} orientations and reported the present hierarchy () > {} > ().[27] However, the photocatalytic behavior was reversed between the ZnO single crystals with the () and {} orientations when two faces were exposed.

In addition, since ZnO NW arrays present a high surface over volume ratio at nanoscale dimensions along with the opportunity to trap the light[8, 28] and to be fixed on a dedicated substrate hence suppressing any filtration step, they are considered as excellent candidates to boost the photocatalytic activity. As such, Zhou et al.[29] and Roza et al.[30] have investigated the effect of the length of ZnO NWs grown by two hydrothermal methods using zinc sulfate and zinc nitrate hexahydrate, respectively, on their photocatalytic activity, which does not significantly depend on their structural morphology. Several physical phenomena including the diffusive transport of organic dyes in the ZnO NW arrays[29] or the light absorption[30] have been proposed, but no one has discussed the influence of the surface selectivity of ZnO NWs in the photocatalytic process.

In this work, we investigate the photocatalysis of the surfaces of ZnO using single crystals with five polar, semipolar, and nonpolar plane orientations, as well as NWs grown by CBD with a length varying in the range of 0–1 μm by adjusting the growth time. The effects of the plane orientation and polarity on the photocatalytic activity and processes of ZnO single crystals and NWs are thoroughly shown and discussed in the light of the diffusive transport of organic dye and light absorption, as well as charge carrier and molecule management forming reactive radicals. The findings allow us to revisit the photocatalytic processes operating on the surfaces of ZnO, opening perspectives to drastically improve their performance.

2 Results

2.1 Photocatalytic Activity and Processes of ZnO Single Crystals with Different Orientations

ZnO single crystals were used as ideal materials to assess the influence of their orientation on the photocatalytic activity and processes. ZnO single crystals with the Zn-polar () +*c*-plane, *O*-polar () –*c*-plane, nonpolar () *m*-plane, semipolar () *r*-plane, and semipolar () plane orientations were prepared using thermal annealing at high temperature under oxygen atmosphere. A schematic of the wurtzite structure of ZnO defining all the different polar, nonpolar, and semipolar planes is represented in **Figure 1a**. The angle between the semipolar () *r*-plane and polar *c*-plane is 42.77°, while the angle between the semipolar () plane and polar *c*-plane is 74.88°. The structural morphology of the surfaces of ZnO single crystals with the different orientations is presented in Figure **1b–f** using atomic force microscopy (AFM) imaging in tapping mode. The surface of the ZnO single crystal with the Zn-polar *c*-plane exhibits a step morphology with a typical height in the range of 2–3 Å,[31-33] roughly corresponding to half of the *c*-lattice parameter of 5.206 Å in ZnO, as seen in Figure **1b**. The first layers of two adjacent terraces are thus occupied by two opposite types of ions. The surface of the ZnO single crystal with the *O*-polar *c*-plane has a step morphology with a typical height in the range of 5–6 Å, corresponding to the *c*-lattice parameter, as seen in Figure **1c**. The step height of annealed polar *c*-plane ZnO single crystals has generally been found to depend on the conditions used. The terrace width of around 1 µm for the ZnO single crystal with the *O*-polar *c*-plane orientation is much larger than the terrace width of about 0.3 µm for the ZnO single crystal with the Zn-polar *c*-plane orientation. The root-mean-square (RMS) roughness of ZnO single crystals with the Zn- and *O*-polar c-plane orientations is about 2.2 and 1.8 Å, respectively. Similarly, the surface of the ZnO single crystal with the *m*-plane orientation has a step morphology with a typical height in the range of 3–4 Å, corresponding to the *a*-lattice parameter of 3.249 Å in ZnO, as seen in Figure **1d**. The step structure is however discontinuous. The RMS roughness of that ZnO single crystal is correlatively slightly higher and reaches the value of around 3.0 Å. In contrast, the surface of the ZnO single crystal with the *r*-plane orientation exhibits no step morphology and is relatively flat with a RMS roughness of around 2.3 Å, as seen in Figure **1e**. Eventually, the surface of the ZnO single crystal with the () plane orientation has no step morphology either, but exhibits a relief that is characteristic of the presence of Zn-rich particles resulting in an increase of the RMS roughness to about 11.4 Å, as seen in Figure **1f**. The wettability of all these ZnO single crystals in contact with deionized water through the determination of contact angle was measured by drop sessile method, as reported in Figure S1, Supporting Information. Interestingly, all the surfaces of ZnO single crystals are hydrophilic, regardless of their polar, nonpolar, or semipolar orientation.

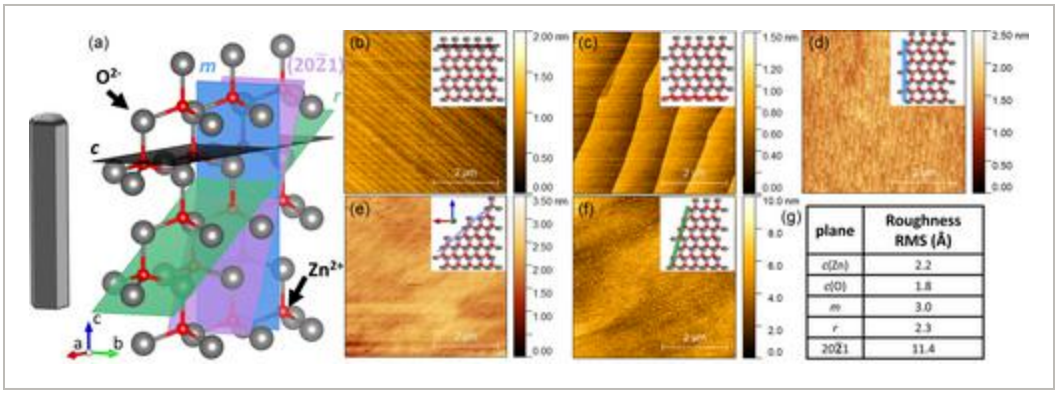

Figure 1

Open in figure viewer | PowerPoint

a) Schematic of the wurtzite structure of ZnO along the Zn-polar *c*-axis, representing the different polar, nonpolar, and semipolar planes considered. AFM maps in tapping mode of ZnO single crystals with the b) Zn-polar () +*c*-plane, c) *O*-polar () –*c*-plane, d) nonpolar () *m*-plane, e) semipolar () *r*-plane, and f) semipolar () plane orientations. The insets represent the schematic of the wurtzite structure of ZnO along the Zn-polar *c*-axis cut parallel to the orientations considered. The small red (resp. large grey) spheres represent the Zn atoms (resp. O atoms). g) RMS roughness of ZnO single crystals with the different orientations.

The photocatalytic activity of ZnO single crystal with the Zn-polar () +*c*-plane orientation as measured under UV-A irradiation with a 12 W/cm^2 LED is presented as a typical example in **Figure** 2a through the evolution of the residual (C) over initial (C_0) concentration ratio of methyl orange (MO) organic dye as a function of time. The UV–vis absorption spectra of MO organic dye during photocatalysis using the ZnO single crystals with the other orientations are reported in Figure S2, Supporting Information. When no ZnO single crystal-based photocatalysts are used, the residual over initial concentration ratio of MO organic dye keeps the same value of around 100% and hence no significant photocatalytic activity occurs. In contrast, the incorporation of ZnO single crystal-based photocatalysts leads to a drastic decrease in the residual over initial concentration ratio of MO organic dye and thus to a strong enhancement of the photocatalytic activity. The decrease in the residual over initial concentration ratio of MO organic dye as presented in Figure 2b is more or less pronounced, depending on the orientation of the ZnO single crystals. Since the initial concentration of MO organic dye is sufficiently low, the photocatalytic degradation kinetics was assessed within the Langmuir–Hinshelwood[13] model describing the surface reaction limited conditions with a Langmuir-type adsorption as follows[34]:

(1)

where k_S is the apparent reaction rate constant and t is the time. All the plots of $\ln(C_0/C)$ versus t for ZnO single crystals with the different orientations exhibit a linear relationship with a high correlation coefficient close to 1, as presented in Figure 2c. This shows that the photocatalytic degradation process of MO organic dye obeys a pseudo-first-order reaction kinetics, regardless of the orientation of ZnO single crystals. The reaction rate is thus proportional to the concentration of MO organic dye, and the surface reaction sites on the ZnO single crystals are not saturated. The slope deduced from each fit gives an estimate of k_S for ZnO single crystals with the different orientations, as reported in Figure 2d. The value of k_S significantly varies in the range of 3.2×10^{-4} to 1.8×10^{-3} min^{-1}, which is delimited by the values for ZnO single crystals with the *O*- and Zn-polar *c*-plane orientations, respectively. Since the size and thickness of ZnO single crystals are the same regardless of their orientations, the amount of catalysts used is the same. The magnitude of the photocatalytic activity of ZnO single crystals with the different orientations is as a result ranked as follows: () < {} < {} < {} < (). The present investigation is in relatively good agreement with Kislov et al. comparing the photocatalytic activity when two sides of the ZnO single crystals were exposed.[27] When only one side of the ZnO single crystal with the *m*-plane orientation was exposed, the photocatalytic activity was however found to be very poor. The present investigation is also consistent with Han et al. including the photocatalytic activity of objects with semipolar plane orientations.[22]

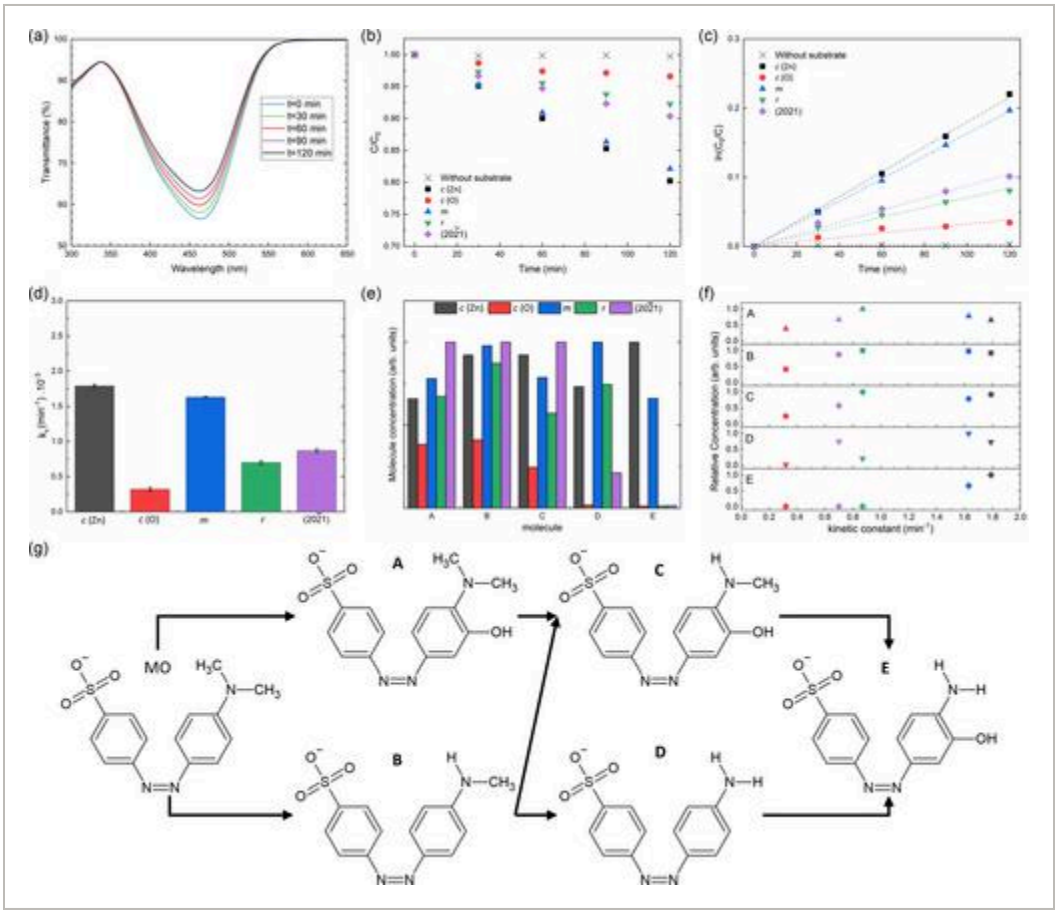

Figure 2

Open in figure viewer | PowerPoint

a) Evolution of UV–vis absorption spectra of MO organic dye during photocatalysis using the ZnO single crystal with the Zn-polar () +*c*-plane orientation. b) Evolution of the residual (*C*) over initial (C_0) concentration ratios of MO organic dye as a function of time for ZnO single crystals with the Zn-polar () +*c*-plane, *O*-polar () –*c*-plane, nonpolar {} *m*-plane, semipolar {} *r*-plane, and semipolar {} semipolar plane orientations. c) Corresponding photocatalytic degradation kinetics plots of MO organic dye. The dashed lines represent the linear fit from the Langmuir–Hinshelwood model in Equation (1). d) Corresponding k_S apparent reaction rate constants for ZnO single crystals with the different orientations. e) Evolution of the different degradation molecule concentrations normalized to the highest concentration value for each of them for ZnO single crystals with the different orientations. f) Evolution of the different degradation molecule concentrations normalized to the highest concentration value for each of them as a function of k_S for each ZnO single crystal. The color code used to identify the nature of ZnO single crystals is similar in b–f). g) Photocatalytic degradation pathways of MO organic dye and nature of the relative degradation molecules generated.

The chemical composition of the solution of MO organic dye after the photocatalytic activity measurements was assessed by ultra-performance liquid chromatography (UPLC) following the experimental procedure reported in Ref. 35. Several wavelength values were used to find the optimal intensity of each peak and the corresponding chromatograms are presented in Figure S3, Supporting Information. From the comparison with Ref. 35, six molecules with retention times of 9, 3.5, 2.8, 1.3, 1.8, and 7.1 min and named as A, B, C, D, E, and MO, respectively, were identified. The nature of each degradation molecule is presented in Figure 2g. It is worth noticing in Figure S4, Supporting Information that the area under the peak corresponding to MO organic dye, determined by UPLC, is highly correlated with the k_S values, determined by UV–vis absorption measurements. The area under each peak is related to the degradation molecule concentration and was normalized to the highest value as presented for ZnO single crystals with the different orientations in Figure 2e. As expected from the photocatalytic degradation kinetics plots, the ZnO single crystals with the *O*- and Zn-polar *c*-plane orientations generate the smallest and largest amount of degradation molecules, respectively. Interestingly, the maximum concentrations of A, B, and C degradation molecules are obtained in the case of the ZnO single crystal with the {} plane orientation, which nevertheless showed half of the photocatalytic activity of the ZnO single crystal with the Zn-polar *c*-plane orientation. To avoid a bias coming from the different kinetics in the degradation processes, the relative concentrations of each degradation molecule are plotted as a function of k_S in Figure 2f. The first expectation would be to get a linear increase in the relative concentrations of each degradation molecule with k_S. However, Cohen et al. showed that the A and B degradation molecules reach a maximum relative concentration around the same time followed by a continuous decrease,[36] which can account for the small difference between the ZnO single crystals with the Zn-polar *c*-plane and *m*-plane orientations. They further found a plateau for

the C degradation molecules prior to the increase in its relative concentration, which could explain the fairly similar amount for the ZnO single crystals with the () plane, Zn-polar *c*-plane and *m*-plane orientations. However, this can also suggest that the surface with the plane orientation promotes another degradation pathway as compared to the surfaces of the Zn-polar *c*-plane and *m*-plane orientations. This assumption can be supported by the corresponding low relative concentration of the D degradation molecules, suggesting that the surface with the {} plane orientation promotes the oxidation of the phenyl ring. Since the E degradation molecules appear in the third step of the degradation pathway, it is expected that the formation process starts later, explaining the absence for the three less active ZnO single crystals. The fact that the ZnO single crystal with the {} plane orientation does not generate the E degradation molecule may indicate that the highest relative concentration of the C degradation molecules is due to the degradation kinetics. As such, either the formation process of the C degradation molecules has not started yet or demethylation of the tertiary amine is limited by the surface with the {} plane orientation. The present investigation overall indicates that the ZnO single crystals with the different orientations do not induce significant changes in the degradation pathways. Therefore, the nature of the radicals generated and involved is the same, apart from the ZnO single crystal with the semipolar {} plane orientation possibly promoting the A and C compounds over the B and D ones.

2.2 Influence of the Growth Time on the Structural Morphology of ZnO NWs

The structural morphology of the polycrystalline ZnO seed layer and of ZnO NWs grown by CBD for a growth time ranging from 0.5 to 4 h is presented in **Figure** 3a using field-emission scanning electron microscopy (FESEM) imaging. Regardless of the growth time, ZnO NWs are vertically aligned following a homoepitaxial growth on the polycrystalline ZnO seed layer that is highly textured along the polar *c*-axis.[37] They exhibit a typical hexagonal shape characteristic of their wurtzite structure oriented along the polar *c*-axis. The mean length and diameter of ZnO NWs were determined from the cross-sectional and top-view FESEM images, respectively, over a population of more than 60 objects. The diameter of ZnO NWs was measured as the distance joining two vertices and crossing its center. The apparent density was estimated by counting the number of ZnO NWs over three 1 × 1 μm^2 surface area from the top-view FESEM images. The evolution of the mean length, mean diameter, aspect ratio, and apparent density of ZnO NWs as a function of growth time is presented in Figure 3b–e. The mean length of ZnO NWs first increases linearly from 82 ± 10 to 915 ± 41 nm as the growth time is increased from 0.5 to 3 h, and then reaches a plateau around the value of 1008 ± 200 nm as the growth time is further increased to 4 h, as seen in Figure 3b. These experimental data are in agreement with Ref. 38 in which the elongation process of ZnO NWs was modeled by solving Fick's diffusion equations. The lower axial growth rate for a longer growth time was explained by the depletion

of the Zn(II) reactant in the chemical bath in a regime limited by its diffusive transport.[38] Instead, the mean diameter of ZnO NWs is fairly constant for a growth time ranging from 0.5 to 1 h, as seen in Figure 3c, owing to the effect of the nucleation process proceeding at the very beginning to form the ZnO nuclei. The mean diameter of ZnO NWs then increases from 42 ± 16 to 64 ± 22 nm as the growth time is increased from 1 to 3 h, and eventually reaches also a plateau around the value of 71 ± 27 nm as the growth time is further increased to 4 h. Interestingly, the aspect ratio of ZnO NWs follows the same behavior as the mean length of ZnO NWs, because the variation of the mean diameter is much less pronounced in comparison, as seen in Figure 3d. In contrast, the apparent density of ZnO NWs continuously decreases from 236 ± 14 to 80 ± 6 NWs μm^{-2} as the growth time is increased from 0.5 to 4 h, as shown in Figure 3e. The high apparent density of ZnO NWs at the very short growth time of 0.5 h when no coalescence process occurs was correlated with the high density of ZnO grains exhibiting the polar and semipolar orientations and acting as nucleation sites in the polycrystalline seed layer.[39] The initial drastic decrease in the apparent density of ZnO NWs originates from the coalescence process of nonperfectly aligned ZnO NWs nucleating on top of ZnO grains exhibiting the semipolar orientations.[39] In contrast, the subsequent less pronounced decrease in the apparent density of ZnO NWs comes from the increase in their diameter. Importantly, the ensemble of ZnO NWs is composed of both Zn- and *O*-polar ZnO NWs in the same array.[40] The number of ZnO NWs with the Zn polarity arising from the top of the array is expected to increase as the growth time is increased owing to their much larger axial growth rate as compared to ZnO NWs with the O polarity.[41] The resulting volume of ZnO NWs over a surface area of 1 μm^2 thus increases from about 25 to 350 nm^3 as the growth time is increased from 0.5 to 4 h.

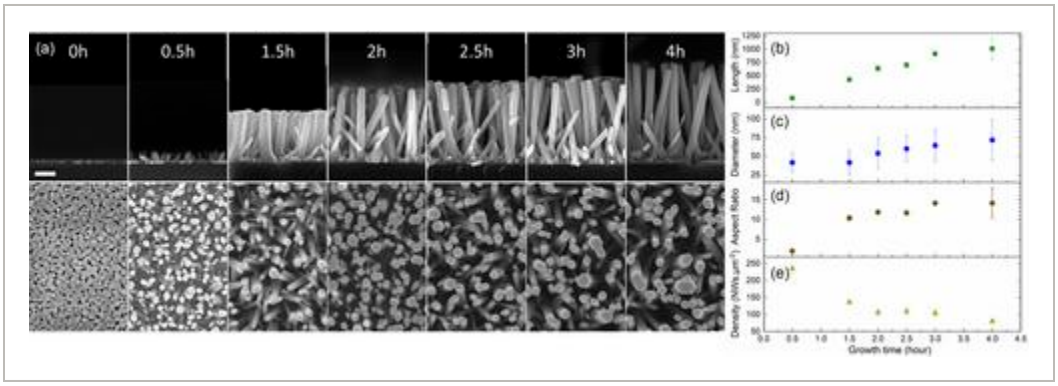

Figure 3

Open in figure viewer | PowerPoint

a) Top-view and cross-sectional view FESEM images of the polycrystalline ZnO seed layer and of ZnO NWs grown by CBD for a growth time ranging from 0.5 to 4 h. The scale bar denoting 200 nm is the same for each top-view and cross-sectional

view FESEM image, respectively. Evolution of the b) mean length, c) mean diameter, c) aspect ratio, and d) apparent density of ZnO NWs as a function of growth time.

2.3 Investigation of the Different Facets in ZnO NWs

The surface areas of the different facets in ZnO NWs were estimated from the morphological properties as reported from FESEM imaging and are expressed over a substrate surface area of one cm^2. ZnO NWs were considered as perfect hexagonal columns. The top surface area was determined from the surface area of one single hexagon multiplied by the apparent density of ZnO NWs. The sidewall surfaces are composed of six rectangles with a width equal to half-of-the diameter of ZnO NWs and a length equal to the length of ZnO NWs. The sidewall surface area was obtained by multiplying the surface area of six rectangles by the apparent density of ZnO NWs. The total surface area (A_{Total}) of ZnO NWs is thus the sum of both the top surface area (A_{Top}) and the sidewall surface area ($A_{Sidewall}$) as follows:

(2)

where r is the radius of ZnO NWs, l is their length, and d_{NW} is their apparent density.

The evolution of the top surface area, sidewall surface area, and total surface area of ZnO NWs as a function of growth time is presented in **Figure 4a**. The top surface area of ZnO NWs first decreases from 0.26 to 0.15 $cm^2.cm^{-2}$ as the growth time is increased from 0.5 to 1.5 h owing to the drop of its density. It then increases progressively from 0.15 to 0.28 $cm^2.cm^{-2}$ as the growth time is further increased to 3 h and eventually saturates for longer growth times owing to coalescence phenomena. This evolution follows the evolution of the mean diameter of ZnO NWs, except at the short growth time of 0.5 h where it is governed by the high apparent density of ZnO NWs. The sidewall surface area of ZnO NWs instead increases continuously from 2.4 to 18.4 $cm^2.cm^{-2}$ as the growth time is increased from 0.5 to 3 h and then saturates around 18 $cm^2.cm^{-2}$ for longer growth times. Its evolution follows the evolution of the mean length of ZnO NWs. Importantly, the total surface area of ZnO NWs is dominated by their sidewall surface area, such that it increases from 2.7 to 18.7 $cm^2.cm^{-2}$ as the growth time is increased from 0.5 to 3 h and then saturates around 18 $cm^2.cm^{-2}$ for longer growth times.

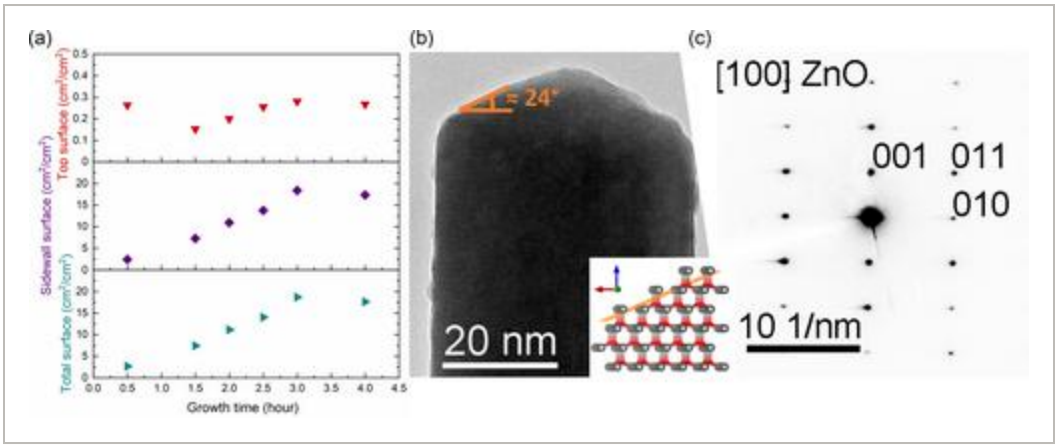

Figure 4

Open in figure viewer | PowerPoint

a) Evolution of the top surface area, sidewall surface area, and total surface area of ZnO NWs grown by CBD as a function of growth time, as determined over a substrate surface area of one cm^2. b) HRTEM image of a single ZnO NW grown by CBD for a growth time of 3 h. The inset is a schematic of the wurtzite structure of ZnO along the Zn-polar *c*-axis cut parallel to the semipolar () plane. c) Corresponding SAED pattern showing its orientation along the polar *c*-axis.

The different facets composing the top and sidewall surfaces are presented in Figure 4b using high-resolution transmission electron microscopy (HRTEM) imaging. The single ZnO NW exhibits a pure single crystalline wurtzite phase with no extended defects and is oriented along the expected polar *c*-axis, as shown in Figure 4c. The top surface is however composed of a flat facet with a small area corresponding to the polar *c*-plane and of an inclined facet with a larger area exhibiting an angle of around 24° that can correspond to the semipolar () plane, as seen in the inset of Figure 4b. The area proportion of both flat and inclined facets varies from NWs to NWs, but it is generally dominated by the semipolar () plane and induced by the fact that the next layer starts developing before the end of the previous one during the growth. In contrast, the sidewall surface is composed of a flat facet with a low roughness, which is perpendicular to the polar *c*-plane and thus corresponds to the expected nonpolar *m*-plane. The elongated hexagonal shape of ZnO NWs grown by CBD and hence the formation of the resulting facets have been explained by thermodynamic and chemical reactivity considerations.[42, 43] Under near-equilibrium growth conditions, the free energy as CBD proceeds should be minimized, favoring the formation of the nonpolar *m*-planes with the lowest surface energy in the wurtzite structure[44] as compared to the more reactive polar *c*-plane with a higher surface energy.[45] The presumable adsorption of HMTA molecules on the nonpolar *m*-plane sidewalls further inhibits to some extent their development as CBD proceeds.[42, 46] Here, the additional formation of the semipolar () plane separating the nonpolar *m*-planes on the sidewalls of ZnO

NWs from the polar *c*-plane on the top may originate from the elongation process and specifically from the regime to develop each polar *c*-plane.

2.4 Influence of the Growth Time on the Photocatalytic Activity of ZnO NWs

The photocatalytic activity of ZnO NW arrays obtained with different growth times was assessed using a similar experimental procedure as the one used for determining the photocatalytic activity of ZnO single crystals. It is reported in **Figure 5a** through the evolution of the residual (C) over initial (C_0) concentration ratio of MO organic dye as a function of time. All the plots of $\ln(C_0/C)$ versus t for ZnO NWs obtained with the different growth times are shown in Figure 5b. They exhibit a linear relationship with a high correlation coefficient close to 1, showing that the photocatalytic degradation process of MO organic dye obeys a pseudo-first-order reaction kinetics regardless of the growth time of ZnO NWs. To make a direct comparison with the ZnO single crystals exhibiting the different orientations, the k_S apparent reaction rate constants expressed in (min^{-1}) and deduced from the linear fit were divided by the substrate surface area and hence expressed in ($min^{-1}.cm^{-2}$). The evolution of k_S as a function of the growth time of ZnO NWs is presented in Figure 5c. k_S keeps a value of around 1.5×10^{-3} $min^{-1}.cm^{-2}$ as the growth time is increased from 0 to 1.5 h and then increases linearly to around 1.8×10^{-3} $min^{-1}.cm^{-2}$ as the growth time is further increased to 3 h. Eventually, k_S decreases back to the value of around 1.5×10^{-3} $min^{-1}.cm^{-2}$ as the growth time reaches 4 h. The present evolution of k_S is consistent with Ref. 30, where the same range of dimensions of ZnO NWs was investigated. It is also worth noticing that the k_S values lie in the range of 1.5–1.8 $\times 10^{-3}$ $min^{-1}.cm^{-2}$, which roughly matches the values of k_S for ZnO single crystals with the Zn-polar *c*-plane and nonpolar *m*-plane orientations. Correlatively, the polycrystalline ZnO seed layer highly textured along the polar *c*-axis exhibits a k_S value of around 1.5×10^{-3} $min^{-1}.cm^{-2}$. In other words, the huge surface area offered by the structural morphology of ZnO NWs does not result in a significant increase in the k_S value, which is in agreement with Ref. 29. To go into more details, the evolution of k_S as a function of the top and sidewall surface areas of ZnO NWs is presented in Figure 5d,e. k_S first increases from 3.2 to 3.9×10^{-3} min^{-1} when the top and sidewall surface areas increase from 0.15 to 0.28 cm^2 and from 7.2 to 18.4 cm^2, respectively. An increase in the top and sidewall surface areas of 87% and 156%, respectively, only leads to an increase in the k_S value of 22%. Subsequently, k_S even decreases slightly to 3.7×10^{-3} min^{-1} when the top and sidewall surface areas reaches 0.27 and 17.3 cm^2, respectively. Finally, it should be noted here that the smaller k_S value deduced for ZnO NWs obtained with a growth time of 0.5 h despite their significant top surface area of about 0.26 cm^2 originates from the presence of *O*-polar ZnO NWs with a poor photocatalytic activity, which are present at the beginning of the CBD process.

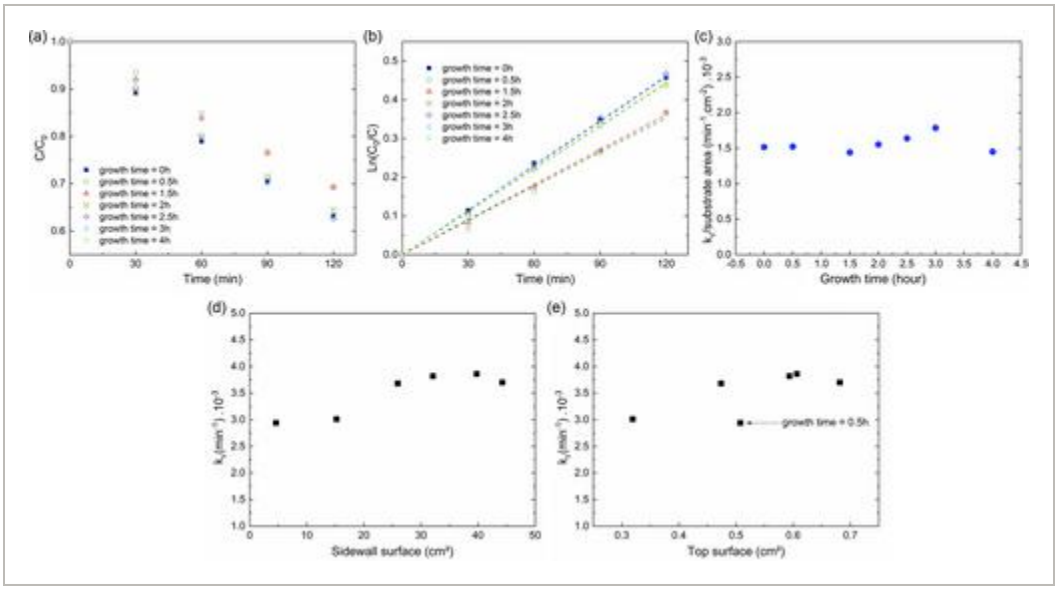

Figure 5

Open in figure viewer | PowerPoint

a) Evolution of the residual (C) over initial (C_0) concentration ratios of MO organic dye as a function of time for the polycrystalline ZnO seed layer and for ZnO NWs grown by CBD for a growth time ranging from 0.5 to 4 h. b) Corresponding photocatalytic degradation kinetics plots of MO organic dye. The dashed lines represent the linear fit from the Langmuir–Hinshelwood model in Equation (1). Evolutions of the k_S apparent reaction rate constant as a function of the c) growth time, d) sidewall surface area, and e) top surface area of ZnO NWs.

2.5 Effect of the MO Organic Dye Penetration on the Photocatalytic Activity of ZnO NWs

To investigate the penetration of MO organic dye by diffusive transport inside the ZnO NW arrays, the approach developed in Ref. 29 using a pore diffusion problem is employed on the basis of the Ternan's method.[47] The method estimates the ratio of the effective diffusivity of a given molecule in a pore filled with a liquid (D_{eff}) over the diffusivity of the same molecule in the bulk solution (D_B) as follows:

(3)

where MO is the molecule considered, $\lambda = r_m/r_p$ for which r_m is the molecule radius and r_p is the pore radius. P is a dimensionless parameter taking the interactions between the solution and pore wall into account as follows:

(4)

where $\beta = r_w/r_p$ for which r_w is the distance from the pore wall in which the solvent has an enhanced viscosity. The same approximation as in Ref. 29 for r_w and r_m was considered, assimilating r_w to the diameter of one water molecule equal to 0.28 nm[48] and r_m to a value of 0.5 nm deduced from the molar volume of 321 cm^3 mol^{-1} using Le Bas additive volumes.[49] The ratio $\Delta\mu_w/\mu_B$ was considered from glucose diffusion in water-filled alumina-silicate pores and estimated as 95.6. To adapt the geometry to the structural morphology of ZnO NWs developed here, r_p was inferred from the FESEM data. From the determination of the top surface area (A_{Top}), the total pore surface area was estimated as 1-A_{Top} and the number of pores is equal to the apparent density (d_{NW}) of ZnO NWs. Thus, the surface area of one pore can be approximated as the total pore surface area divided by the apparent density of ZnO NWs. If the pore is assumed to be a perfect circle, r_p is obtained from:

(5)

The values of r_p and D_{eff}/D_B are reported in **Figure** 6a. It is worth noticing that the values of r_p increase from 32 to 54 nm as the growth time of ZnO NWs is increased from 0.5 to 4 h and lie in the same order of magnitude as the mean distance separating two nearby ZnO NWs. The values of D_{eff}/D_B are pretty low and increase from 0.17 to 0.26 as the growth time of ZnO NWs is increased from 0.5 to 4 h. This suggests that the diffusion process of MO organic dye in the ZnO NW array may be limited, regardless of the growth time used.

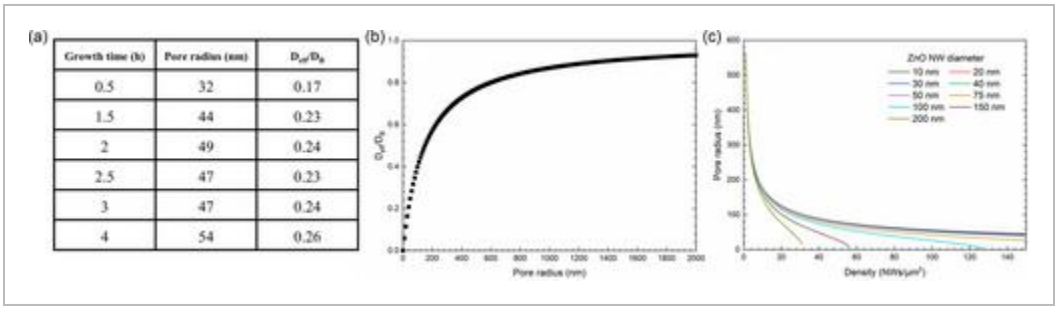

Growth time (h)	Pore radius (nm)	D_{eff}/D_B
0.5	32	0.17
1.5	44	0.23
2	49	0.24
2.5	47	0.23
3	47	0.24
4	54	0.26

Figure 6

Open in figure viewer | PowerPoint

a) Pore radius and D_{eff}/D_B ratio of MO organic dye for different growth times of ZnO NWs by CBD. b) Evolution of the D_{eff}/D_B ratio as a function of pore radius. c) Evolution of the pore radius as a function of the apparent density of ZnO NWs for different mean diameters.

To design the optimal architecture of ZnO NW arrays favoring the penetration of MO organic dye, D_{eff}/D_B was plotted as a function of r_p, as presented in Figure 6b. As an example, to get a value of D_{eff}/D_B higher than 0.70 or 0.95 corresponding to a medium or maximum diffusion process of MO organic dye, r_p should be larger than 350 or 2860 nm, respectively. The

evolution of r_p as a function of the apparent density of ZnO NWs is reported in Figure 6c and plotted for the different values of the mean diameter of ZnO NWs ranging from 10 to 200 nm. By setting the minimum r_p value to 350 nm, the optimal apparent density of ZnO NWs is of around 3 NWs μm^{-2} and relatively independent upon their mean diameter. The present value is from one to two orders of magnitude lower than the apparent density of ZnO NWs typically reported using the spontaneous growth approach by CBD as described in the present investigation.

To overcome the limitations coming from the spontaneous growth approach and to significantly decrease the apparent density of ZnO NWs, the selective area growth (SAG) approach using nano-imprint lithography (NIL) with a silicon 0.5 × 0.5 cm^2 mask exhibiting a periodic network of holes separated by a distance of one micrometer each other was performed. Ordered ZnO NR arrays over a silicon 0.5 × 0.5 cm^2 substrate were prepared by the SAG approach using two different growth times of 1 h 05 min and 1 h 45 min. Their structural morphology along with their photocatalytic activity was compared with those of spontaneous grown ZnO NWs for a growth time of 1 h 45 min over a silicon 0.5 × 0.5 cm^2 substrate. The structural morphology of ordered ZnO NR arrays is presented in **Figure** 7a,b. More than one single ZnO NR can grow from each hole, and exhibit a moderate vertical alignment owing to the numerous ZnO grains with the polar and semipolar orientations acting as nucleation sites in the polycrystalline seed layer. The structural morphology of spontaneously grown ZnO NW arrays is comparable with the one presented in Figure 1. All the dimensions of ordered and spontaneously grown ZnO NRs and NWs were estimated from FESEM images following the same approach as described previously and are reported in Figure 7c. Here, the total surface area of ZnO NRs is still dominated by the sidewall surface area, which is around 30 times larger than the top surface area. Since the apparent density of ordered ZnO NRs is around 7 NRs.μm^{-2}, the D_{eff}/D_B value is expected to be around 0.56 in both cases. In contrast, the apparent density of spontaneously grown ZnO NWs of around 117 NWs μm^{-2} is related to an expected D_{eff}/D_B value of around 0.2. The diffusion process of MO organic dye in the ordered ZnO NR arrays should thus be greatly enhanced and hence promote the photocatalytic activity of the sidewall surfaces mainly composed of the nonpolar *m*-planes. In addition, the inclined-ordered ZnO NRs should also promote the access of MO organic dye to the sidewall surfaces and favor the UV light penetration through efficient scattering processes. The evolutions of the residual (C) over initial (C_0) concentration ratio of MO organic dye as a function of time along with the corresponding plots of $\ln(C_0/C)$ versus t for both ordered and spontaneously grown ZnO NW arrays are presented in Figure 7d,e, respectively. The photocatalytic activity is pretty close with a degradation rate of MO organic dye of around 5% for ordered ZnO NR arrays and around 7% for spontaneously grown ZnO NW arrays. Accordingly, the k_S values lie in the range of 4.1–5.1 $\times 10^{-4}$ min^{-1} for ordered ZnO NR arrays and reach 6.8 $\times 10^{-4}$ min^{-1} for spontaneously grown ZnO NW arrays. In other words, favoring the access of MO organic dye to the sidewall

surfaces of ZnO NRs and NWs that are mainly composed of the nonpolar *m*-planes does not result in a significant enhancement of the photocatalytic activity.

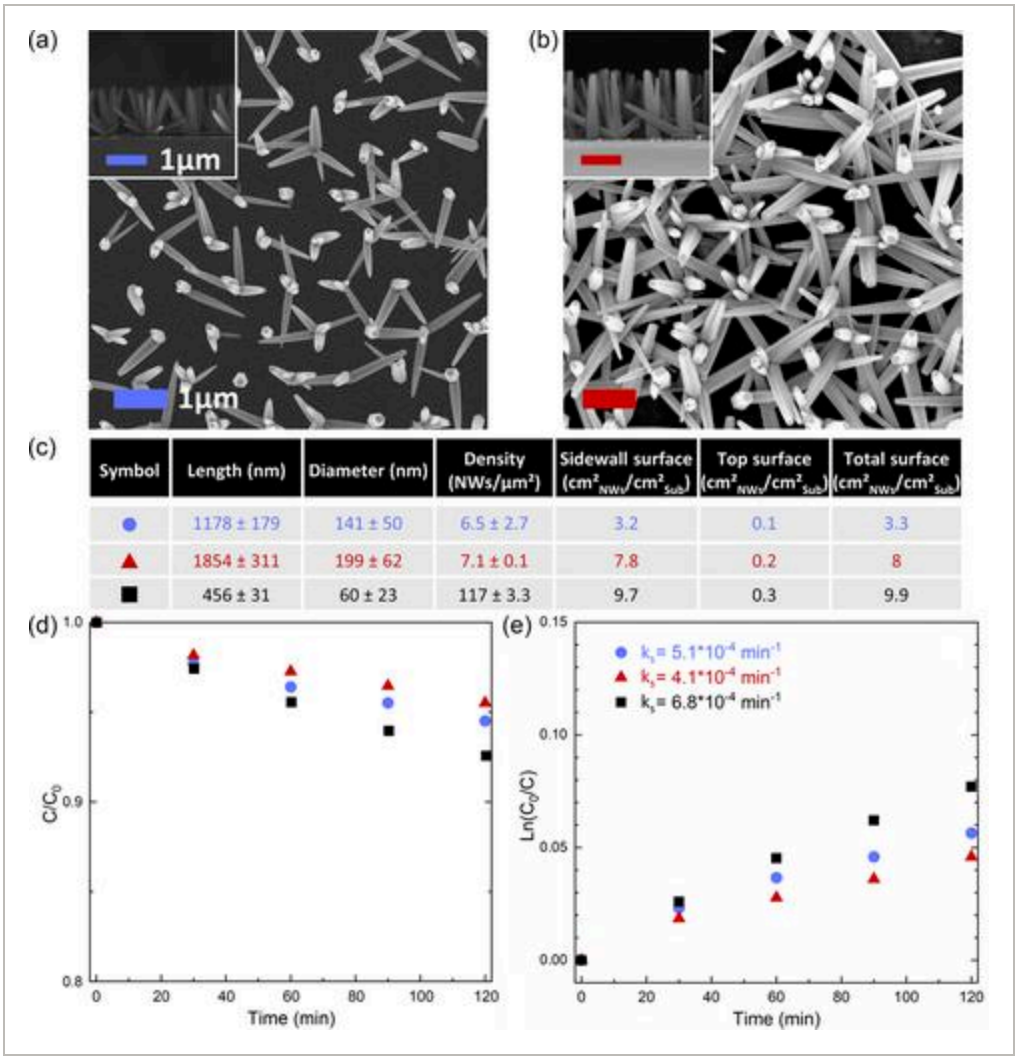

Figure 7

Open in figure viewer | PowerPoint

a) Top-view and cross-sectional view FESEM images of ordered ZnO NR arrays grown by CBD for a growth time of 1 h 05 min and b) 1 h 45 min. The scale bar denoting 1 µm is the same for each top-view and cross-sectional view FESEM image, respectively. c) Mean length, diameter, density, sidewall surface area, top surface area, and total surface area of ordered ZnO NRs and spontaneously grown ZnO NWs. d) Evolution of the residual (C) over initial (C_0) concentration ratios of MO organic dye as a function of time for ordered ZnO NR arrays and spontaneously grown ZnO NW arrays. e) Corresponding photocatalytic degradation kinetics plots of MO organic dye. The symbols (•) and (▲) stand for ordered ZnO NR arrays grown for 1 h 05 min and 1 h 45 min, respectively, while the symbol (▪) stand for spontaneously grown ZnO NWs for 1 h 45 min.

3 Discussion

The magnitude of the photocatalytic activity of ZnO single crystals with the different orientations follows the present ranking: () > {} > {} > {} > (). Basically, the photocatalytic process is governed by the capacity of charge carriers (i.e., h_{VB}^{+} and e_{CB}^{-}) generated under UV light and of molecules (i.e., H_2O, $OH_{(ads)}$, $O_{2(ads)}$) to reach the surface of ZnO where they react together to form reactive radicals (i.e., $^{\bullet}OH$ and $^{\bullet}O_2^{-}$) decomposing the MO organic dye. The present capacity strongly depends on the polar, semipolar or nonpolar orientation of ZnO and the electronic properties of the related surfaces depending on the surrounding environment.[20, 50, 51] First, the migration of charge carriers toward the sites where the photocatalytic process operates is affected by the band bending on the actual surfaces of ZnO, which has highly been debated theoretically and experimentally over the last two decades but on the ideal and clean surfaces. The clean surfaces of ZnO single crystals with the *O*- and Zn-polar *c*-plane orientations are known to exhibit an upward band bending, while those of ZnO single crystals with the *m*-plane orientation have a downward band bending.[52] Since the photocatalytic process operates in water, the different surfaces of ZnO are stabilized by hydroxylation processes.[53, 54] The hydroxyl termination of ZnO single crystal with the *O*-polar *c*-plane orientation originates from hydrogen atoms attached to the outer plane of O atoms. The hydroxyl termination of ZnO single crystal with the Zn-polar *c*-plane orientation comes from O–H groups bonded to the outer plane of Zn atoms. In contrast, since the ZnO single crystal with the *m*-plane orientation possesses an equal number of O and Zn atoms on the outer plane, it is assumed that both hydrogen atoms and O–H groups take part in the hydroxyl termination. However, the simultaneous presence of O and Zn atoms on the same surface may favor synergistic effects, as reported for the adsorption of H_2 with one hydrogen linked to each atom in air.[55] In the case of ZnO single crystals with the semipolar plane orientations like (), the simultaneous presence of O and Zn atoms on the surface[56] should induce a photocatalytic behavior similar to the ZnO single crystal with the *m*-plane orientation. Nevertheless, the chemical stability of ZnO with the semipolar plane orientation is known to be less pronounced than ZnO with the *m*-plane orientation and thus their photocatalytic behavior is closer to that of ZnO with the polar plane orientation with less reactive terminations. The concentration of hydrogen and O–H groups favoring the hydroxyl termination is supposed to depend on the semipolar character of ZnO single crystal, exhibiting a different number of O and Zn atoms on the outer plane. As a result, the hydroxyl terminations acting as electron donors are responsible for the downward band bending of the different surfaces of ZnO single crystals, where a surface electron accumulation layer is confined.[57] A semiconductor-to-metal transition proceeds on the different surfaces of hydroxylated ZnO single crystals.[58] Interestingly, the magnitude of the downward band bending depends on the coverage with hydroxyl terminations. It is more pronounced for the ZnO single crystal with the Zn-polar *c*-plane orientation than for the ZnO single crystal with the *O*-polar *c*-plane orientation and to a lesser extent for the ZnO single

crystal with the *m*-plane orientation.[57] In other words, the free e_{CB}^- more readily reaches the surface of the ZnO single crystal with the Zn-polar *c*-plane orientation than the surfaces of the ZnO single crystal with the *O*-polar *c*-plane or *m*-plane orientations and reacts with adsorbed O_2 molecules, possibly accounting for its greater photocatalytic activity. Second, the supply of species and molecules required for the reaction with charge carriers on the surfaces of ZnO is dependent upon the nature of the orientation of ZnO single crystals. The increase in the concentration of O–H groups is likely favorable for activating the formation of reactive radicals. In that sense, the ZnO single crystal with the Zn-polar *c*-plane orientation is supposed to exhibit more O–H groups providing $^{\bullet}OH$ radicals by reacting with trapped h_{VB}^+ for instance as compared to the ZnO single crystal with the *O*-polar *c*-plane orientation, likely accounting for its greater photocatalytic activity. Furthermore, additional physical and chemical phenomena are expected to proceed, including the effects of surface charges correlated through electrostatic interactions and a shift of the valence band maximum position affecting the reduction potential of the different planes.[59] A significant variation of the lattice parameters between the bulk and surfaces of ZnO may also play a role, as recently shown in the case of Cu_2O crystals.[60]

The small dependence of the photocatalytic activity of ZnO NWs on their length varying in the broad range of 0–1 μm is not due to any issues related to the penetration of MO organic dyes in the arrays or to the penetration of UV light, as shown from the data collected on selective area grown ZnO NRs using NIL. An important finding of the present investigation is thus that the sidewalls of ZnO NWs composed of nonpolar *m*-planes are relatively inactive in the photocatalytic process as compared to the corresponding ZnO single crystal with the same nonpolar *m*-plane orientation. The striking difference between the ZnO NWs and single crystals may originate from several physical and chemical phenomena at work during the photocatalytic process. First, the structural morphology of the surface of the ZnO single crystal with the *m*-plane orientation strongly differs from the structural morphology of the surface of ZnO NWs. The surface of the ZnO single crystal as revealed in Figure 1 is relatively rough and exhibits a discontinuous structure of steps with a height corresponding to the *a*-lattice parameter. In contrast, the surface of ZnO NWs, as shown in Figure 4, is relatively flat with no step structure. Second, the chemical composition of the surface of ZnO single crystal with the *m*-plane orientation should be distinguished from the chemical composition of the surface of ZnO NWs. The surface of the ZnO single crystal is perfectly clean with no chemical residues (*e.g.*, organic compounds), owing to its preparation at high temperature under oxygen atmosphere. The thermal annealing above 1000 °C is also known to eliminate the potential hydrogen and nitrogen-related defects.[61] In contrast, the surface of ZnO NWs grown by CBD at low temperature contains chemical adsorbates like O–H and N–H groups, as well as HMTA molecules and its residues presumably adsorbing on the nonpolar *m*-plane sidewalls. Moreover, nonintentionally doped ZnO NWs grown by CBD contain a high concentration of hydrogen-[62] and nitrogen-related defects,[63] affecting the properties of their different

surfaces. Third, in contrast to ZnO single crystals with a low doping level exhibiting a surface electron accumulation layer, ZnO NWs with a much higher doping level are known to exhibit a surface electron depletion region and hence an upward band bending on their nonpolar *m*-plane sidewalls.[64] As such, the free h_{VB}^{+} (and not the free e_{CB}^{-}) more readily reaches the surface of ZnO NWs, likely activating different photocatalytic processes.[65] In other words, both the distinct structural morphology and chemical composition of the surfaces of ZnO NWs as well as their much higher doping level are expected to modify the photocatalytic processes at work. In addition, the present finding indicates that the nature of the physical or chemical deposition techniques needs to be carefully considered when comparing the photocatalytic process of ZnO NWs,[24] and any differences in the growth procedure should be taken into account. This certainly accounts for the controversy in the literature about the photocatalytic activity of the different planes of ZnO as a function of the shape of nanostructures for instance, for which different deposition techniques and growth procedure have been used. The different exposed surfaces of ZnO single crystals and NWs are eventually crucial to enhance the photocatalytic activity and tune the photocatalytic processes, opening the way for designing original architectures with tailored facets.[66]

4 Conclusion

The photocatalytic processes operating on ZnO single crystals with five different polar, semipolar, and nonpolar plane orientations and prepared at high temperature have thoroughly been explored. The photocatalytic activity follows a pseudo-first-order kinetics, regardless of the plane orientation involved, and it is significantly enhanced as follows: () < {} < < {} < (). The photocatalytic processes are independent upon the orientation of the planes of ZnO single crystals using UPLC, apart from the semipolar () orientation, and discussed via the capacity of charge carriers and molecules to reach the surface where they react to form reactive radicals. The structural morphology of ZnO NWs investigated by HRTEM imaging reveals the formation of nonpolar *m*-planes on their sidewalls and of a mix of the polar *c*-plane and semipolar () plane on their top. Additionally, the photocatalytic activity of ZnO NWs has been found to be relatively independent upon their length, showing that the increase in their surface area is not sufficient to boost the photocatalytic performance. The noncorrelation between the surface area of ZnO NWs and their photocatalytic activity has deeply been studied from the data collected on selective area grown ZnO NRs using NIL. It has been revealed that the present statement is neither due to the penetration of MO organic dye in the arrays, nor to the penetration of UV light. Instead, the sidewalls of ZnO NWs composed of the nonpolar *m*-planes are much less efficient than the ZnO single crystal with the same nonpolar *m*-plane plane orientation, indicating that the structural morphology and chemical composition of the surface as well as their much higher doping level govern the photocatalytic activity and processes. These findings

identify the current limitations of ZnO NWs grown by CBD and open the way for designing efficient strategies aiming at strongly improving their photocatalytic performance.

5 Experimental Section

Preparation and Deposition Techniques

The ZnO single crystals with the Zn-polar () +*c*-plane, *O*-polar () –*c*-plane, semipolar () *r*-plane, and semipolar () plane orientations were provided from Crystec. The ZnO single crystal with the nonpolar () *m*-plane orientation was provided from Tokyo Denpa. The surface areas of all ZnO single crystals were of 1 × 1 cm^2. The surfaces of ZnO single crystals were prepared by thermal annealing at high temperature under oxygen atmosphere. (001) silicon substrates were used as substrates for the spontaneous growth and SAG of ZnO NWs and NRs, respectively. They were first cleaned in an ultrasonic bath with acetone and isopropyl alcohol to remove the residual contaminants. The polycrystalline ZnO seed layers were deposited by dip coating using a sol–gel process as described in Ref. 42 and used as unpatterned for the spontaneous growth of ZnO NWs and as patterned for the SAG of ZnO NRs using nanoimprint lithography (NIL). The patterned polycrystalline ZnO seed layers were coated with a 150 nm-thick PMMA layer using spin coating. A silicon 0.5 × 0.5 cm^2 mask exhibiting a periodic network of rods with a mean diameter and length of 80 and 115 nm, respectively, and separated by a distance of one micrometer each other was used for proceeding with NIL. The patterned polycrystalline ZnO seed layers were subsequently etched with an Evactron RF plasma system using an oxygen plasma with a pressure of 0.4 Torr and a RF power of 12 W to remove the residual PMMA in the periodic network of holes. The spontaneous growth and SAG of respective ZnO NWs and NRs were achieved by CBD in sealed reactors containing a chemical precursor solution composed of zinc nitrate hexahydrate [$Zn(NO_3)_2{\cdot}6H_2O$, Sigma-Aldrich] and hexamethylenetetramine [HMTA, $C_6H_{12}N_4$, Sigma-Aldrich] with an equimolar concentration of 30 mM in deionized water. The sealed reactors were placed in an oven heated at 90 °C for a growth time varying in the range of 30 min to 4 h.

Structural Characterization Techniques

The morphology of the surface of ZnO single crystals with the different orientations was characterized with a BRUKER Icon Dimension AFM instrument in tapping mode and analyzed with Gwyddion software. The morphology of ZnO NWs and NRs was assessed with a ZEISS Gemini 300 FESEM instrument using an in-lens detector and an acceleration voltage of 5 keV. The nature of the different planes composing ZnO NWs was identified using transmission electron microscopy (TEM) imaging. ZnO NWs were scratched from the silicon substrates with a diamond tip and dispersed on a copper grid. HRTEM images and selected area electron

diffraction (SAED) patterns were collected with a JEOL 2010 LaB_6 microscope operating at 200 kV with a 0.19 nm point-to-point resolution.

Chemical and Photocatalytic Characterization Techniques

The photocatalytic activity of 1 × 1 cm^2 ZnO single crystals with the different orientations and of ZnO NWs and NRs over 1.5 × 1.5 and 0.5 × 0.5 cm^2 silicon substrate areas, respectively, was assessed by investigating the degradation processes of MO as organic dye. The set-up was composed of a UV LED emitting at a wavelength of 365 ± 10 nm with an irradiance of 12 $W.cm^{-2}$ over a range of 75 × 20 mm^2 (FireJet ONE, Phoseon Technology), a stirring plate, and a 40 mL crystallizer covered by a watch glass to avoid any evaporation processes. The samples were placed on a UV-polymerized resin holder at a distance of 20 cm below the UV LED. To avoid the parasitic reactions on the backside of the samples, the backside of ZnO single crystals was covered with a tape while the backside of silicon substrates with ZnO NWs was cleaned with a hydrochloric acid solution. The solution volume was set to 30 mL with a MO organic dye initial concentration of 10 $\mu mol.L^{-1}$. To reach the adsorption process equilibrium, the samples were left in the MO organic dye solution for 1 h in the dark. The degradation process of MO organic dye as a function of time was followed by measuring the absorbance at 465 nm obtained from UV–vis absorption measurements with a PerkinElmer Lambda 950 UV–vis spectrophotometer in the range of 300–650 nm. The MO organic dye solution was taken and put in 3 mL quartz cuvettes each 30 min for 2 h and then put back in the crystallizer. The UV LED was switched off during the UV–vis absorption measurements. The nature of the degradation molecules generated by the photocatalytic processes was investigated using an Agilent UPLC system equipped with a Luna omega 3 µm PS C-18 100 Å column. The column dimensions were of 150 mm in length and 3 mm in inner diameter. The mobile phase used for the chromatographic separation was prepared by mixing phosphate and acetonitrile in an 80/20 ratio. The pH of the mobile phase was adjusted at 6.8 throughout the analysis following the approach by Baiocchi et al.[35] The spectral data were acquired at multiple wavelengths, specifically at 360, 430, 460, and 485 nm, to facilitate the identification and quantification of the degradation molecules.

Acknowledgements

The authors acknowledge the financial support from the French Research National Agency through the DOSETTE (ANR-17-CE24-0003) and IMINEN (ANR-22-CE09-0032) projects. This research has further benefited from some of the characterization equipments of Grenoble INP-CMTC platform and of IUT 1 Chemical Department platform. The authors also acknowledge the support by the French RENATECH network through the CIME and PTA technological platforms in Grenoble.

Conflict of Interest

The authors declare no conflict of interest.

Open Research

Data Availability Statement

The data that support the findings of this study are available from the corresponding author upon reasonable request.

Supporting Information

Filename	Description
sstr202300540-sup-0001-SuppData-S1.pdf 1,020.8 KB	Supplementary Material

Please note: The publisher is not responsible for the content or functionality of any supporting information supplied by the authors. Any queries (other than missing content) should be directed to the corresponding author for the article.

References

1 European Environment Agency, in *European Waters: Assessment of Status and Pressures*, Publications Office, LU 2018, EEA Report, ISBN: 978-92-9213-947-6.

Google Scholar

2 L. Persson, B. M. Carney Almroth, C. D. Collins, S. Cornell, C. A. de Wit, M. L. Diamond, P. Fantke, M. Hassellöv, M. MacLeod, M. W. Ryberg, P. Søgaard Jørgensen, P. Villarrubia-Gómez, Z. Wang, M. Z. Hauschild, *Environ. Sci. Technol.* 2022, **56**, 1510.

CAS | PubMed | Web of Science® | Google Scholar

3 A. Tkaczyk, K. Mitrowska, A. Posyniak, *Sci. Total Environ.* 2020, **717**, 137222.

CAS | PubMed | Web of Science® | Google Scholar

4 European Environment Agency, in *Beyond Water Quality: Sewage Treatment in a Circular Economy*, Publications Office, LU 2022, EEA Report.

Google Scholar

5 M. Salimi, A. Esrafili, M. Gholami, A. Jonidi Jafari, R. Rezaei Kalantary, M. Farzadkia, M. Kermani, H. R. Sobhi, *Environ. Monit. Assess.* 2017, **189**, 414.

PubMed | Web of Science® | Google Scholar

6 S. Lim, J. L. Shi, U. Von Gunten, D. L. McCurry, *Water Res.* 2022, **213**, 118053.

CAS | PubMed | Google Scholar

7 M. Mehrjouei, S. Müller, D. Möller, *Chem. Eng. J.* 2015, **263**, 209.

CAS | Web of Science® | Google Scholar

8 Y. Liu, J. Han, W. Qiu, W. Gao, *Appl. Surf. Sci.* 2012, **263**, 389.

CAS | Web of Science® | Google Scholar

9 J. Herney-Ramirez, M. A. Vicente, L. M. Madeira, *Appl. Catal. B Environ.* 2010, **98**, 10.

CAS | Web of Science® | Google Scholar

10 M. Umar, H. A. Aziz, M. S. Yusoff, *Waste Manag.* 2010, **30**, 2113.

CAS | PubMed | Web of Science® | Google Scholar

11 T. E. Agustina, H. M. Ang, V. K. Vareek, *J. Photochem. Photobiol. C Photochem. Rev.* 2005, **6**, 264.

CAS | Web of Science® | Google Scholar

12 K. M. Lee, C. W. Lai, K. S. Ngai, J. C. Juan, *Water Res.* 2016, **88**, 428.

CAS | PubMed | Web of Science® | Google Scholar

13 M. Behnajady, N. Modirshahla, R. Hamzavi, *J. Hazard. Mater.* 2006, **133**, 226.

CAS | PubMed | Web of Science® | Google Scholar

14 A. Fujishima, K. Honda, *Nature* 1972, **238**, 37.

CAS | PubMed | Web of Science® | Google Scholar

15 R. Comparelli, E. Fanizza, M. Curri, P. Cozzoli, G. Mascolo, R. Passino, A. Agostiano, *Appl. Catal. B Environ.* 2005, **55**, 81.

CAS | Web of Science® | Google Scholar

16 C. Xu, L. Cao, G. Su, W. Liu, H. Liu, Y. Yu, X. Qu, *J. Hazard. Mater.* 2010, **176**, 807.

CAS | PubMed | Web of Science® | Google Scholar

17 C. N. C. Hitam, A. A. Jalil, *J. Environ. Manage.* 2020, **258**, 110050.

CAS | PubMed | Web of Science® | Google Scholar

18 V. Nain, M. Kaur, K. S. Sandhu, R. Thory, A. Sinhmar, *Int. J. Biol. Macromol.* 2020, **162**, 24.

CAS | PubMed | Web of Science® | Google Scholar

19 K. Govender, D. S. Boyle, P. B. Kenway, P. O'Brien, *J. Mater. Chem.* 2004, **14**, 2575.

CAS | PubMed | Web of Science® | Google Scholar

20 J. Zúñiga-Pérez, V. Consonni, L. Lymperakis, X. Kong, A. Trampert, S. Fernández-Garrido, O. Brandt, H. Renevier, S. Keller, K. Hestroffer, M. R. Wagner, J. S. Reparaz, F. Akyol, S. Rajan, S. Rennesson, T. Palacios, G. Feuillet, *Appl. Phys. Rev.* 2016, **3**, 041303.

Web of Science® | Google Scholar

21 A. Mclaren, T. Valdes-Solis, G. Li, S. C. Tsang, *J. Am. Chem. Soc.* 2009, **131**, 12540.

CAS | PubMed | Web of Science® | Google Scholar

22 X.-G. Han, H.-Z. He, Q. Kuang, X. Zhou, X.-H. Zhang, T. Xu, Z.-X. Xie, L.-S. Zheng, *J. Phys. Chem. C* 2009, **113**, 584.

CAS | Web of Science® | Google Scholar

23 T.-J. Liu, Q. Wang, P. Jiang, *RSC Adv.* 2013, **3**, 12662.

CAS | Web of Science® | Google Scholar

24 D. Li, H. Haneda, *Chemosphere* 2003, **51**, 129.

CAS | PubMed | Web of Science® | Google Scholar

25 Y. Zheng, C. Chen, Y. Zhan, X. Lin, Q. Zheng, K. Wei, J. Zhu, Y. Zhu, *Inorg. Chem.* 2007, **46**, 6675.

CAS | PubMed | Web of Science® | Google Scholar

26 S. Baruah, M. A. Mahmood, M. T. Z. Myint, T. Bora, J. Dutta, *Beilstein J. Nanotechnol.* 2010, **1**, 14.

CAS | PubMed | Web of Science® | Google Scholar

27 N. Kislov, J. Lahiri, H. Verma, D. Y. Goswami, E. Stefanakos, M. Batzill, *Langmuir* 2009, **25**, 3310.

CAS | PubMed | Web of Science® | Google Scholar

28 O. L. Muskens, S. L. Diedenhofen, B. C. Kaas, R. E. Algra, E. P. A. M. Bakkers, J. Gómez Rivas, A. Lagendijk, *Nano Lett.* 2009, **9**, 930.

CAS | PubMed | Web of Science® | Google Scholar

29 Q. Zhou, J. Wen, P. Zhao, W. Anderson, *Nanomaterials* 2017, **7**, 9.

PubMed | Google Scholar

30 L. Roza, V. Fauzia, M. Y. A. Rahman, *Surf. Interfaces* 2019, **15**, 117.

CAS | Web of Science® | Google Scholar

31 H.-J. Ko, M.-S. Han, Y.-S. Park, Y.-S. Yu, B.-I. Kim, S. S. Kim, J.-H. Kim, *J. Cryst. Growth* 2004, **269**, 493.

CAS | Web of Science® | Google Scholar

32 S. Graubner, C. Neumann, N. Volbers, B. K. Meyer, J. Bläsing, A. Krost, *Appl. Phys. Lett.* 2007, **90**, 042103.

CAS | Web of Science® | Google Scholar

33 H. Maki, N. Ichinose, S. Sekiguchi, N. Ohashi, T. Nishihara, H. Haneda, J. Tanaka, *Jpn. J. Appl. Phys.* 1999, **38**, 2741.

CAS | Web of Science® | Google Scholar

34 B. Ohtani, *J. Photochem. Photobiol. C* 2010, **11**, 157.

CAS | Web of Science® | Google Scholar

35 C. Baiocchi, M. C. Brussino, E. Pramauro, A. B. Prevot, L. Palmisano, G. Marcì, *Int. J. Mass Spectrom.* 2002, **214**, 247.

CAS | Web of Science® | Google Scholar

36 M. Cohen, N. Ferroudj, A. Combes, V. Pichon, S. Abramson, *J. Environ. Chem. Eng.* 2019, **7**, 102987.

CAS | Google Scholar

37 S. Guillemin, V. Consonni, E. Appert, E. Puyoo, L. Rapenne, H. Roussel, *J. Phys. Chem. C* 2012, **116**, 25106.

CAS | Web of Science® | Google Scholar

38 C. Lausecker, B. Salem, X. Baillin, V. Consonni, *J. Phys. Chem. C* 2019, **123**, 29476.

CAS | Web of Science® | Google Scholar

39 T. Cossuet, H. Roussel, J.-M. Chauveau, O. Chaix-Pluchery, J.-L. Thomassin, E. Appert, V. Consonni, *Nanotechnology* 2018, **29**, 475601.

PubMed | Web of Science® | Google Scholar

40 S. Guillemin, R. Parize, J. Carabetta, V. Cantelli, D. Albertini, B. Gautier, G. Brémond, D. D. Fong, H. Renevier, V. Consonni, *Nanotechnology* 2017, **28**, 095704.

PubMed | Web of Science® | Google Scholar

41 T. Cossuet, E. Appert, J.-L. Thomassin, V. Consonni, *Langmuir* 2017, **33**, 6269.

CAS | PubMed | Web of Science® | Google Scholar

42 R. Parize, J. Garnier, O. Chaix-Pluchery, C. Verrier, E. Appert, V. Consonni, *J. Phys. Chem. C* 2016, **120**, 5242.

CAS | Web of Science® | Google Scholar

43 K. M. McPeak, T. P. Le, N. G. Britton, Z. S. Nickolov, Y. A. Elabd, J. B. Baxter, *Langmuir* 2011, **27**, 3672.

CAS | PubMed | Web of Science® | Google Scholar

44 A. Wander, F. Schedin, P. Steadman, A. Norris, R. McGrath, T. S. Turner, G. Thornton, N. M. Harrison, *Phys. Rev. Lett.* 2001, **86**, 3811.

CAS | PubMed | Web of Science® | Google Scholar

45 C. Tang, M. J. S. Spencer, A. S. Barnard, *Phys. Chem. Chem. Phys.* 2014, **16**, 22139.

CAS | PubMed | Web of Science® | Google Scholar

46 A. Sugunan, H. C. Warad, M. Boman, J. Dutta, *J. Sol–Gel Sci. Technol.* 2006, **39**, 49.

CAS | Web of Science® | Google Scholar

47 M. Ternan, *Can. J. Chem. Eng.* 1987, **65**, 244.

CAS | Web of Science® | Google Scholar

48 R. Netrabukkana, K. Lourvanij, G. L. Rorrer, *Ind. Eng. Chem. Res.* 1996, **35**, 458.

CAS | Web of Science® | Google Scholar

49 B. E. Poling, J. M. Prausnitz, J. P. O'Connell, in *The Properties of Gases and Liquids*, McGraw-Hill, New York 2001.

Google Scholar

50 C. Woll, *Prog. Surf. Sci.* 2007, **82**, 55.

CAS | Web of Science® | Google Scholar

51 J. Goniakowski, F. Finocchi, C. Noguera, *Rep. Prog. Phys.* 2008, **71**, 016501.

CAS | Web of Science® | Google Scholar

52 K. Ozawa, K. Mase, *Phys. Rev. B* 2011, **83**, 125406.

CAS | Web of Science® | Google Scholar

53 R. Heinhold, G. T. Williams, S. P. Cooil, D. A. Evans, M. W. Allen, *Phys. Rev. B* 2013, **88**, 235315.

CAS | Web of Science® | Google Scholar

54 R. Heinhold, S. P. Cooil, D. A. Evans, M. W. Allen, *J. Phys. Chem. C* 2014, **118**, 24575.

CAS | Web of Science® | Google Scholar

55 A. Wander, N. M. Harrison, *J. Phys. Chem. B* 2001, **105**, 6191.

CAS | Web of Science® | Google Scholar

56 J.-M. Chauveau, Y. Xia, I. Ben Taazaet-Belgacem, M. Teisseire, B. Roland, M. Nemoz, J. Brault, B. Damilano, M. Leroux, B. Vinter, *Appl. Phys. Lett.* 2013, **103**, 262104.

CAS | Web of Science® | Google Scholar

57 A. R. McNeill, A. R. Hyndman, R. J. Reeves, A. J. Downard, M. W. Allen, *ACS Appl. Mater. Interfaces* 2016, **8**, 31392.

CAS | PubMed | Web of Science® | Google Scholar

58 A. Calzolari, M. Bazzani, A. Catellani, *Surf. Sci.* 2013, **607**, 181.

CAS | Web of Science® | Google Scholar

59 M. C. Toroker, D. K. Kanan, N. Alidoust, L. Y. Isseroff, P. Liao, E. A. Carter, *Phys. Chem. Chem. Phys.* 2011, **13**, 16644.

CAS | PubMed | Web of Science® | Google Scholar

60 B. Chen, G. Kumar, Y. Wei, H. Ma, J. Kao, P. Chou, Y. Chuang, I. Chen, J. Chou, Y. Lo, M. H. Huang, *Small* 2023, **19**, 2303491.

CAS | Web of Science® | Google Scholar

61 J. Villafuerte, F. Donatini, J. Kioseoglou, E. Sarigiannidou, O. Chaix-Pluchery, J. Pernot, V. Consonni, *J. Phys. Chem. C* 2020, **124**, 16652.

CAS | Web of Science® | Google Scholar

62 A. Janotti, C. G. Van de Walle, *Nat. Mater.* 2007, **6**, 44.

CAS | PubMed | Web of Science® | Google Scholar

63 J. Villafuerte, O. Chaix-Pluchery, J. Kioseoglou, F. Donatini, E. Sarigiannidou, J. Pernot, V. Consonni, *Phys. Rev. Mater.* 2021, **5**, 056001.

CAS | Google Scholar

64 A. M. Lord, T. G. Maffeis, M. W. Allen, D. Morgan, P. R. Davies, D. R. Jones, J. E. Evans, N. A. Smith, S. P. Wilks, *Appl. Surf. Sci.* 2014, **320**, 664.

CAS | Web of Science® | Google Scholar

65 P. Gaffuri, T. Dedova, E. Appert, M. Danilson, A. Baillard, O. Chaix-Pluchery, F. Güell, I. Oja-Acik, V. Consonni, *Appl. Surf. Sci.* 2022, **582**, 152323.

CAS | Web of Science® | Google Scholar

66 M. H. Huang, M. Madasu, *Nano Today* 2019, **28**, 100768.

CAS | Web of Science® | Google Scholar